GPU-Accelerated Large-Eddy Simulations of High-Speed Cavity Flows With Dynamic Doors Deployment

GPU-accelerated large-eddy simulations of high-speed cavity flows with dynamic doors deployment

Guillaume A. Brès[*], Christopher B. Ivey[†], Liam Heidt[‡], Kan Wang[§], Sanjeeb T. Bose[†],

Cadence Design Systems, Inc., San Jose, CA 95134, USA

Romain Hottois[¶]

Cadence Design Systems, Inc., 1170 Watermael-Boitsfort, Belgium

and

Joel Guerrero[‖], Tony Di Fabbio[‖]

Leonardo S.p.A, 16151 Genova, Italy

GPU-accelerated wall-modeled large-eddy simulations of the M219 cavity benchmark are performed at Mach $M_\infty = 0.6$, 0.85 and 1.35 for open rectangular cavities of length-to-depth ratio $L/D = 5$ and 10. Wall-pressure predictions are compared to available Kulite measurements on the cavity floor and show good agreement in terms of tonal noise frequency and amplitude, as well as broadband noise levels and streamwise distribution of pressure fluctuations along the cavity. In particular, the experimental trends for Mach number effect, and cavity aspect ratio dependence and onset of self-sustained Rossiter resonance are well captured in the computations. An additional simulation is performed with generic cavity doors added to the M219 cavity configuration: the inclusion of the opened doors tends to change the dominant mode selected, shift the frequency of the tones present, and increases the magnitude of the pressure fluctuations on the floor of the cavity. As a proof-of-concept demonstration of a novel general-motion capability, the dynamic deployment of the doors is also simulated. Analysis of the opening sequence suggests that weak signature of the first two Rossiter tones becomes detectable around door angle of 30°, before the resonant mechanism gets fully established when the doors are opened beyond 55°.

Nomenclature

c	Speed of sound
D	Cavity depth
f	Frequency
L	Cavity length
M	Mach number
P	Pressure
Re	Reynolds number
St	Strouhal number
T	Temperature
t	Time
U	Streamwise velocity
u	Fluid velocity vector
W	Cavity width
x,y,z	Cartesian coordinates
δ_{99}	Boundary layer thickness
γ	Specific heat ratio
ϕ	Door opening angle
θ	Boundary layer momentum thickness

Subscript

∞	Free-stream property
avg	time-averaged quantity
rms	root-mean-square quantity
t	Total (stagnation) property

[*]Software Engineering Group Director - Cascade R&D
[†]Distinguished Engineer - Cascade R&D
[‡]Lead Software Engineer - Cascade R&D
[§]Sr. Principal Software Engineer - Cascade R&D
[¶]Sr. Application Engineer
[‖]Leonardo, Labs

I. Introduction

High-speed flow over open cavity is prevalent to a number of aircraft components, including landing gear wells and weapon bays. Self-sustained oscillation and high pressure fluctuations inside the cavity can affect aircraft aerodynamics, structural integrity of components and store separation process. As reviewed by Lawson & Barakos [1], cavity flow has been the subject of many experimental and computational studies over the years. Dating back to early experimental works on canonical rectangular cut-out [2, 3, 4], cavity oscillations in compressible flow are typically described as a flow-acoustic resonance mechanism: small instabilities in the shear layer interact with the downstream corner of the cavity and generate acoustic waves, which propagate upstream and create new disturbances in the shear layer. Resonance occurs at a given frequency when the disturbances lead to reinforcement and ultimately saturation. In the 1960's, Rossiter [3] developed the now classic semi-empirical formula to predict the resonant frequencies,

$$St_n = \frac{f_n L}{U_\infty} = \frac{n-\alpha}{M_\infty + 1/\kappa} \qquad n = 1, 2, 3... \tag{1}$$

where L is the cavity length, $M_\infty = U_\infty/c_\infty$ is the free-stream Mach number, and St_n is the Strouhal number corresponding to the n-th Rossiter mode frequency f_n. In deriving equation 2, Rossiter assumed the speed of sound in the cavity to be the free-stream speed of sound, which is a reasonable assumption for subsonic flows but introduces larger errors at high Mach. To improve the predictions in higher Mach number range, Heller [4] proposed a modified formula where the cavity sound speed is assumed to be equal to the free-stream stagnation sound speed:

$$St_n = \frac{f_n L}{U_\infty} = \frac{n-\alpha}{M_\infty/\sqrt{1+(\gamma-1)M_\infty^2/2} + 1/\kappa} \qquad n = 1, 2, 3... \tag{2}$$

The non-dimensional empirical constants α and κ are a phase delay and an average convection speed of vortical disturbances in the shear layer, respectively. The typical values used in the literature are $\kappa = 0.57$, $\alpha = 0.25$ for $L/D \leq 4$ and linear interpolation of the original data from Rossiter [3] for $4 \leq L/D \leq 10$, where D is the cavity depth (see table 1).

L/D	≤ 4	6	8	10
α	0.25	0.38	0.54	0.58

Table 1: Averaged phase delay as a function of cavity aspect ratio [3].

Many of the early numerical studies focused on direct numerical simulations (DNS) of canonical 2D and 3D rectangular cavities at lower Reynolds number [5, 6], because of constraints on geometrical complexity and computational cost. With advancements in high-performance computing, meshing techniques and numerical methods, simulations of high-speed cavity flows at high Reynolds number are now within reach for more realistic cavity shapes, including internal structures [7], store separation [8], and cavity with doors [9, 10, 11, 12, 13].

Generally the presence of doors, when in their open position, increases the magnitude of the pressure fluctuations on the floor and aft wall of the cavity [9, 10, 11]. Only at an almost-closed angle, where the doors impede the resonant mechanism, is the noise reported as quieter than the non-door configuration [10, 11]. This amplification in noise has been attributed to a more two-dimensional flow-field [1, 11], which results in more coherent fluctuations that increase the overall intensity of the resonance. The addition of doors was also seen to modify the relative amplitude of the tones and shift the frequency of the tones present [10, 11]. However, the impact of doors is not always consistent throughout the literature. Murray & Jansen [9] reported that while open doors increased the magnitude of the fluctuations, they completely eliminated the resonant mechanism. Loupy *et al.* [13] found that the geometry of the doors played a critical role in whether doors attenuated or amplified the noise.

The study of dynamic door deployment has been much more limited than its static counterpart, likely due to the numerical challenges and increased computational cost associated with these simulations. Sheta *et al.* [10] and Loupy *et al.* [13] both investigated the impact of door opening on the flow and acoustics. Sheta *et al.* found strong pressure fluctuations begin to develop as the shear layer begins to impinge on the aft wall. Loupy *et al.* [13] reported that the faster the doors open the greater the unsteady loads that are

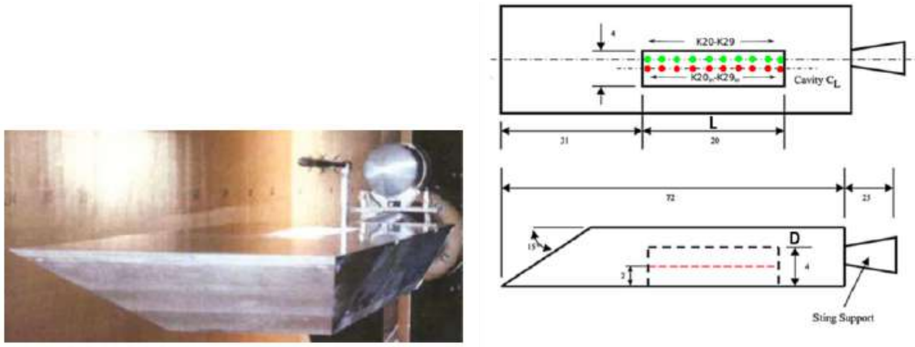

(a) Cavity in wind tunnel [18] (b) Schematic with Kulite locations [17]

Figure 1: M219 cavity model [14] (dimensions in inch)

generated. Additional research into the associated mechanics and physics is needed to better understand this complex phenomenon.

To support such applications, general motion capabilities are being implemented in the compressible flow solver "Fidelity™ Charles" (originally developed by Cascade Technologies, now part of Cadence Design Systems), using a novel mesh generation approach based on Voronoi diagrams. The objective is to leverage wall-modeled large-eddy simulation (LES) methods combined with acceleration from graphic processing unit (GPU) hardware to enable fast, high-fidelity simulation of realistic cavity configurations, including prediction of the unsteady loads and acoustic fluctuations during the doors deployment.

The present study focused first on the M219 cavity experiment [14] which is a classic cavity flow benchmark for CFD [15, 16, 17]. Large-eddy simulations are performed for high-speed flows at Mach $M_\infty = 0.6$, 0.85 and 1.35 over rectangular cavities of aspect ratio $L/D = 5$ and 10, for comparison against the corresponding experimental database. Then, additional simulations are conducted where generic cavity doors are included and deployed dynamically as a demonstration of the general motion capabilities.

II. Description of the M219 cavity configuration

A. Experimental setup

The M219 cavity configuration [14] is shown in figure 1. The rectangular cavity has fixed length $L = 20$ in and width $W = 4$ in, while the depth can be varied from $D = 2$ to 4 in, corresponding to either the shallow ($L/D = 10$) or deep ($L/D = 5$) cavity configuration. The experiments were conducted in the ARA wind-tunnel of test section 9ft×8ft, at free-stream Mach numbers $M_\infty = 0.6$, 0.85 and 1.35, within a range of tunnel total pressure $P_t = 100320$ to 101210 Pa and tunnel total temperature $T_t = 302.2$ to 311.35 K. The cavity location is offset by 1 in from the rig centerline, its start is $x = 0.7874$ m downstream of the flat plate leading edge and the corresponding Reynolds number is $Re_x = \mathcal{O}(1 \times 10^7)$. A transition trip made of sparsely distributed ballotini of 0.15 mm diameter is included in the model at 40mm aft of the leading edge of the plate, with streamwise width of 4 mm. Assuming the development of a turbulent boundary layer along the flat plate, the thickness and momentum thickness of the compressible boundary layer at the start of the cavity can be estimated to $\delta_{99} \approx 0.012$ m and $\theta \approx 0.0012$ m. For cavity flows, the other important parameters typically reported are L/θ, the Reynolds number based on cavity depth Re_D and based on incoming boundary layer momentum thickness Re_θ: for the present case, $L/\theta \approx 430$, $Re_D \approx 6 \times 10^5$ to 1.5×10^6 and $Re_\theta \approx 1300$ to 1900.

The experimental data consists of pressure time histories measured at 10 Kulite regularly distributed on the floor of the empty cavity[a]. The unsteady pressure data is sampled at 6 kHz for 20 blocks of size 1024 samples (i.e., block period of 0.17067 s), which yields a maximum duration of 3.41 s (assuming no block overlap). Note that the Kulites are located either along the rig centerline (green dots in figure 1) for the deep $L/D = 5$ cavity, or along the cavity centerline (red dots in figure 1) for the shallow $L/D = 10$ cavity.

[a] Access to the experimental data was limited to the RMS pressure at the 10 Kulites reported in table 3 of reference [14]. For the Kulite-averaged PSD spectra, the data was digitized from reference [17].

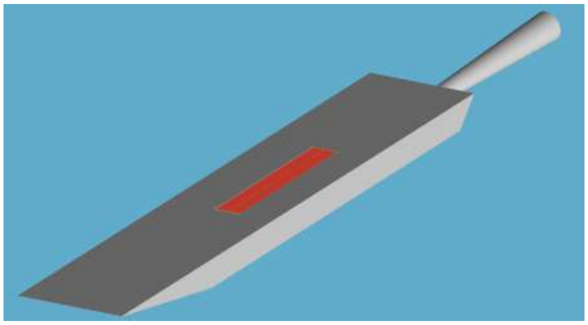

(a) Doors closed ($\phi = 0°$)

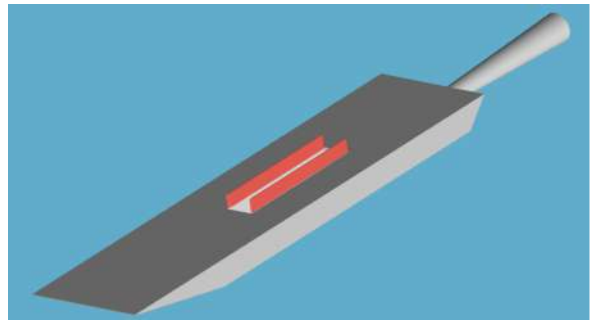

(b) Doors opened ($\phi = 90°$)

Figure 2: M219 cavity configuration with additional generic doors highlighted in red.

B. Numerical setup

For the M219 cavity benchmark, the simulations are performed with the GPU-accelerated compressible flow solver Charles on static grids. The computational domain includes the full rig with the cavity and the sting support, as well as the whole wind-tunnel test section. The rectangular domain extends from $(x, y, z) = (-5, -1.35, -1.22)$ m to $(10, 1.35, 1.22)$ m and the rig is centered with the leading edge at $x = 0$. All the simulations are conducted at the same total pressure $P_t = 100320$ Pa and total temperature $T_t = 302$ K, consistent with the reported experimental range [14]. The free-stream pressure P_∞, temperature T_∞ and streamwise velocity U_∞ are then computed from the isentropic equations and imposed as initial conditions and boundary conditions at the inlet of the computational domain to achieve the desired free-stream Mach numbers M_∞ and match the test conditions. A slip wall boundary condition is used on wind tunnel walls and an adiabatic wall-stress modeling [19, 20] is applied to all other internal surfaces. A Navier-Stokes characteristic boundary condition (NSCBC) with specified free-stream pressure is employed at the outlet of the computational domain, along with an acoustic sponge layer (applied in the volume to damp out acoustic waves away from the geometry) to avoid spurious reflections at the boundaries. The Vreman [21] sub-grid model is used to account for the physical effects of the unresolved turbulence on the resolved flow.

A configuration with generic doors added to the M219 cavity model is also considered (see figure 2) and simulated using the general-motion version of the Charles solver. The door geometry follows the model in Sheta et al. [10] with double chamfer leading edges to weaken the shocks at the door leading edges. Sheta et al. [10] reported that weapon bay doors of Northrop Grumman's YF-23 fighter open in about 2.1s and estimated a representative opening speed for fighter aircraft at high speed: for a typical length of a weapon bay door $L = 1$ m, their estimate of the Strouhal number is approximately 2.87×10^{-4}. Here, the door rotational speed is set to 0.1564 rev/s to match this Strouhal number at the freestream Mach number $M_\infty = 0.85$, and it takes 1.6 s to rotate the doors from the fully closed position ($\phi = 0°$) to the fully opened ($\phi = 90°$) position. In total, the deployment computation simulates 1.8 s with the doors remaining static in the first and last 0.1s respectively.

C. Meshing approach

The unstructured mesh is generated through the computation of Voronoi diagrams [22] as a flexible way of efficiently and robustly partitioning 3D space: given a set of generating points distributed at specific locations with desired density, the Voronoi diagram uniquely defines the cell volume as the region of space closest to each generating point relative to all other generating points in term of Euclidean distance (see example schematic in figure 3). Therefore, the Voronoi paradigm reduces the problem of mesh generation to the much simpler problem of specifying the generating point locations, i.e., the locations where the solution will be sampled. The actual mesh (volumes, faces, topology, neighbor connectivity) is simply a unique mathematical consequence of this choice based on the definition of the Voronoi diagram. This dramatically simplifies the control over local mesh resolution—an important consideration for automation and high-fidelity simulations. Additionally, the discretization of the boundary surface is independent from the near-boundary mesh resolution, allowing arbitrary coarsening or refinement relative to the local surface length scales.

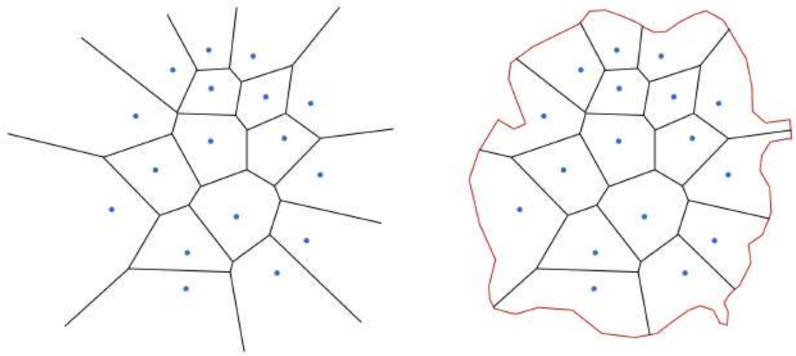

(a) Points only (b) Points and surface

Figure 3: Illustration of Voronoi diagrams in 2D, given a set of generating points (blue dots) and a clipping surface (red lines).

The Voronoi mesh architecture supports a part-based approach for building computational models of complex industrial systems. A large, complicated geometry can be broken up into a series of parts (similar to CAD geometries), where each part prescribes a surface and a set of generating points. The mesh is formed by joining the parts: i.e., intersecting the surfaces and tie-breaking the points. This approach enables a library of parts, each with a unique boundary-fitted grid, to be re-used with different kinematics in multiple simulation campaigns without the tedium of re-meshing the full system geometry for each case.

This platform is extremely flexible as the generating points can be time-dependent, making it a natural method for handling moving geometries where individual surfaces move relative to one another, as in the door deployment considered in the present work. Unlike overset techniques which rely on interpolation to exchange flow information between overlapping grids, the present approach generates a single conformal mesh at each time step using Voronoi diagrams, and the volumes deform continuously based on relative motion of the degrees of freedom. This results in a fully conservative formulation without any interpolation at mesh interfaces. The compressible fluxes are discretized using an arbitrary Eulerian–Lagrangian (ALE) finite volume method that modifies the convective velocity at each Voronoi face by subtracting the local mesh velocity [23]. For example, the relative flux of a scalar ψ through face i is written:

$$F\left(\psi\right)_i = \iint_{\mathcal{S}_i} \psi\left(\vec{u} - \vec{w}\right) \cdot \hat{n}_i \, dS \tag{3}$$

where $\vec{u}$ is the fluid velocity, $\vec{w}$ is the mesh velocity, n_i is face i's outward pointing unit normal and $\mathcal{S}_i$ is face i's surface patch. The ALE approach allows the Voronoi mesh points to move at arbitrary speed independent of the flow velocity. Formally, skew-symmetric operators are employed to conserve kinetic energy in the inviscid, zero Mach number limit, and the scheme also approximately preserves entropy in the inviscid, adiabatic limit, placing the ALE discretization within a kinetic energy and entropy preserving framework.

To ensure discrete conservation, the geometric conservation law (GCL) [24] must be satisfied at every time step. The GCL is a statement of conservation of volume and can be written discretely as:

$$\frac{V^{n+1} - V^n}{\Delta t} = \sum_i \iint_{\mathcal{S}_i} \vec{w} \cdot \hat{n}_i \, dS \tag{4}$$

where V is the discrete Voronoi volume at two different time levels, and the mesh flow rate through face i is given by $\iint_{\mathcal{S}_i} \vec{w} \cdot \hat{n}_i \, dS$. In general, the mesh flow rate computed from knowledge of the part motion and discretely corrected to ensure GCL is satisfied in each cell. Fortunately, the correction is zero in large parts of the mesh, making it relatively efficient to solve. This moving mesh discretization satisfies the geometric conservation law at every single time step, enabling the design of conservative numerical schemes. When cells are added or removed during the simulation (as occurs during door deployment with full surface contact), an implicit discretization is employed to handle the associated stiffness and ensure robust time advancement.

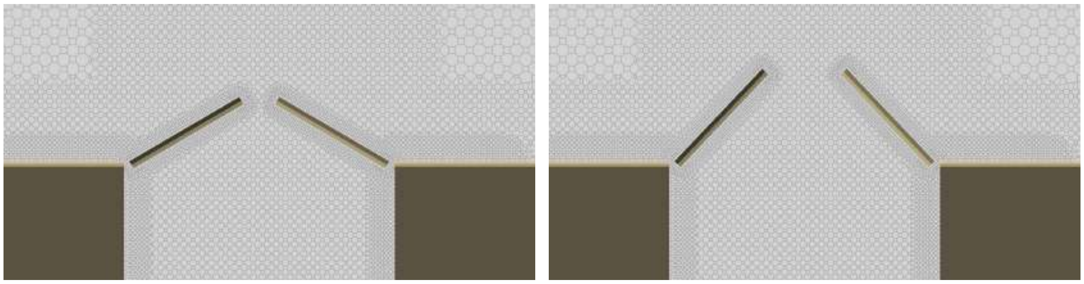

Figure 4: Computational mesh in a plane perpendicular to the door rotation axes at two time instants illustrating the Voronoi mesh methodology for general motion.

In previous works, the mesh motion was restricted to rigid body rotations where the interface between the stationary and moving parts is effectively "sliding" (a rotating disk for instance) and there are no appearing or disappearing degrees of freedom. Under these simplifications, only restricted rebuilds of the Voronoi diagram are required: the mesh rebuilding step reduces to performing an update of the Voronoi diagram faces on the moving-stationary interface only, while the bulk of the mesh remains unchanged. This efficient approach yields substantial speedup for applications such as rotating turbomachinery [23, 25, 26, 27] and propeller flows [28].

In the present work, the meshing methodology is extended to support general motion without the constraints of previous implementations. This includes arbitrary motion paths, appearing/disappearing cells, and full surface contact. This is applied to the dynamic opening of cavity doors, as illustrated in figure 4. Over the course of the moving mesh simulation, cell faces can change orientation and area; they can be created and destroyed, which changes the nearest neighbors of the cells. Furthermore, active cells can disappear and previously blanked cells can reappear as the door surface sweeps through the domain. However, over the course of these topological changes, the Voronoi diagrams remain C^1 continuous in time, so its time derivative can be taken, allowing a fully conservative moving mesh discretization on Voronoi diagrams. Both the surface cutting operations and the flow solution are performed entirely on GPU, enabling efficient simulation of these complex moving boundary problems.

III. LES results for the M219 cavity benchmark

As discussed in Appendix, an initial grid resolution study was performed and the same meshing strategy is applied to both the deep and shallow cavity configurations, and used at all operating conditions $M_\infty = 0.6$, 0.85 and 1.35. For the refined mesh, the grid size is approximately 57 million control volumes (Mcv) for the deep cavity and is slightly reduced to 51 Mcv for the shallow cavity because of the smaller cavity volume.

After the initial transient is flushed, data for the flow statistics and wall-pressure fluctuation analysis is collected at a sampling rate of $10,000$ Hz, for at least 0.5 s. Such simulation time corresponds to 25 periods at 50 Hz (i.e., the lowest frequency of interest) and at least 50 periods of the first Rossiter mode resonant frequency from equation 2. A bin-averaged power spectral density (PSD), with a bin size $\Delta f = 20$ Hz, is computed from the pressure-time history recorded in the simulations at the 10 Kulite locations. The wall-pressure PSD is ensemble-averaged for all Kulite transducers and compared to published data in figures 5 and 6, for the deep $L/D = 5$ and shallow $L/D = 10$ cavity configuration, respectively. The figures also include the pressure rms distribution (in dB, relative to $P_{ref} = 20 \times 10^{-6}$ Pa) at the 10 evenly-spaced Kulites as a function of the normalized streamwise location x/L on the cavity floor.

Overall, the LES results show good agreement with the measurements for all configurations and operating conditions. The Kulite-averaged PSD closely match the measurement in terms of tone frequency and amplitude, as well as broadband levels over most of frequency range of interest, $50 \leq f \leq 3000$ Hz. The main discrepancies are at higher frequencies above 2000 Hz where the measurement levels tend to drop off (likely due to hardware limitations) while the LES predictions show a more regular decay of the wall-pressure fluctuations. For the streamwise distribution of pressure rms along the cavity floor, the LES predictions are typically within ± 1 dB at most Kulite locations. In particular, the experimental trends for Mach number effect, and cavity aspect ratio dependence and onset of self-sustained Rossiter resonance are well captured in the simulations, as discussed in more details the next sections.

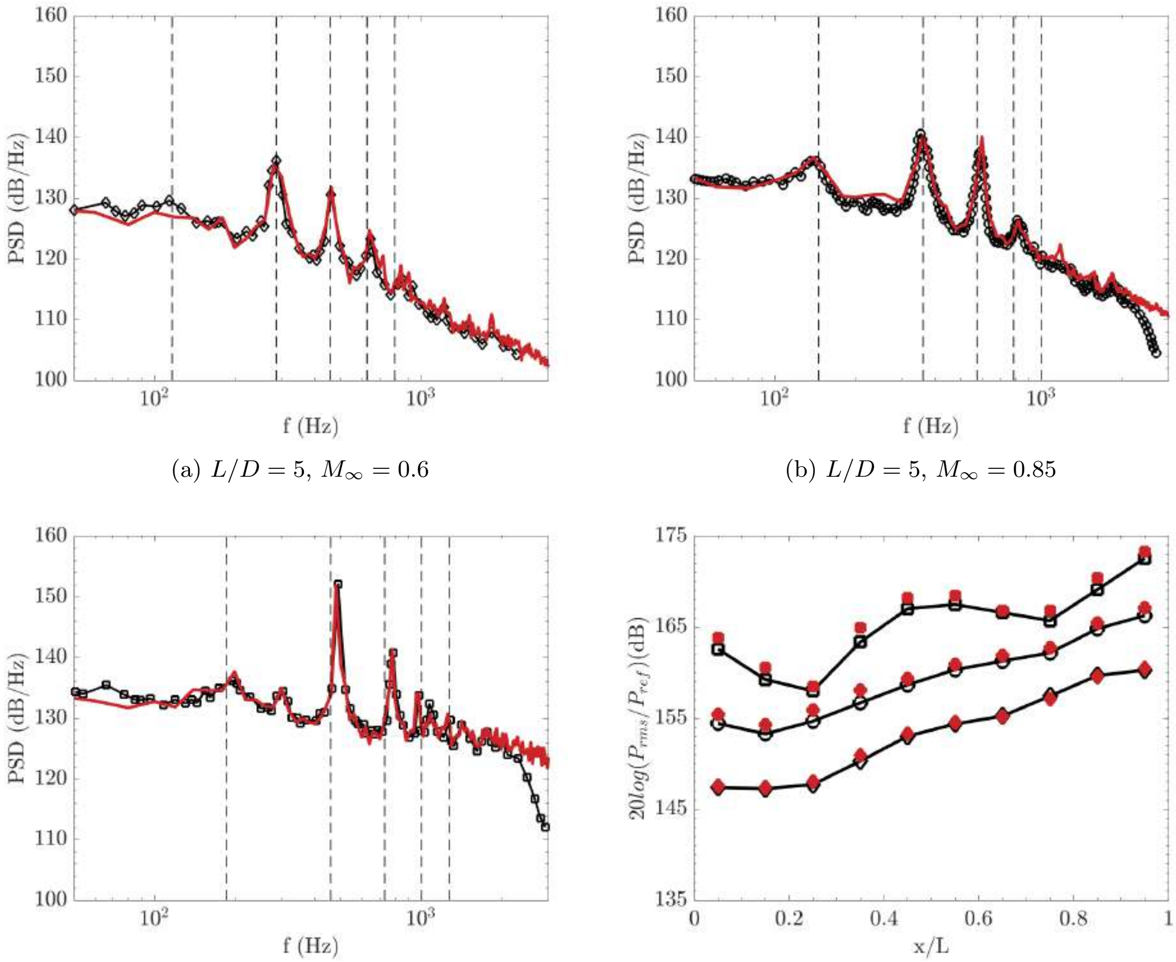

(a) $L/D = 5$, $M_\infty = 0.6$

(b) $L/D = 5$, $M_\infty = 0.85$

(c) $L/D = 5$, $M_\infty = 1.35$

(d) $L/D = 5$, P_{rms} distribution.

Figure 5: Kulite-averaged wall-pressure PSD and P_{rms} distribution along the cavity floor for the deep $L/D = 5$ cavity configuration at Mach $M_\infty = 0.6$ ($-\diamond-$), 0.85 ($-\circ-$) and 1.35 ($-\square-$): **Experiment**; LES. The vertical lines represent the frequency of the first 5 Rossiter modes from equation 2.

A. Effects of cavity aspect ratio

As reported by Tracy & Plentovich [29], the behavior of cavity under transonic flow can change from resonant to non-resonant as the cavity aspect ratio increases. To illustrate the differences in flow physics between the deep and shallow cavity configuration, visualization of the instantaneous flow at Mach $M_\infty = 0.85$ is presented in figures 7. The figure shows the instantaneous pressure field flow in the cavity centerline plane (insert image), and the flow field from the flap plate leading edge to the cavity and the wall shear stress τ_{wall} on the rig and cavity walls. For all the visualizations, the color ranges are kept constant, i.e., from 0.85 (black) to 1.1 (white) for P/P_∞, from 0 (blue) to 1 (red) for M_∞ on the isocontours on Q-criterion and from 0 (black) to 150 Pa (white) for τ_{wall}. For both configuration, the flow quickly transitions close to the rig leading edge, leading the development of a turbulent boundary layer towards the cavity. Inspection of the velocity field just upstream of the cavity confirmed turbulent boundary layer profiles with thickness and momentum thickness consistent with the theoretical values estimated in section IIA.

For the deep cavity at $L/D = 5$, this configuration is representative of open-flow (or "resonant") cavity: the main feature is the aeroacoustic feedback loop mechanism described in the introduction, leading to high levels of broadband wall-pressure fluctuations and strong tones at the resonant frequencies. As shown in figure 5(b), the predicted power spectra density (PSD) show good agreement with the experimental

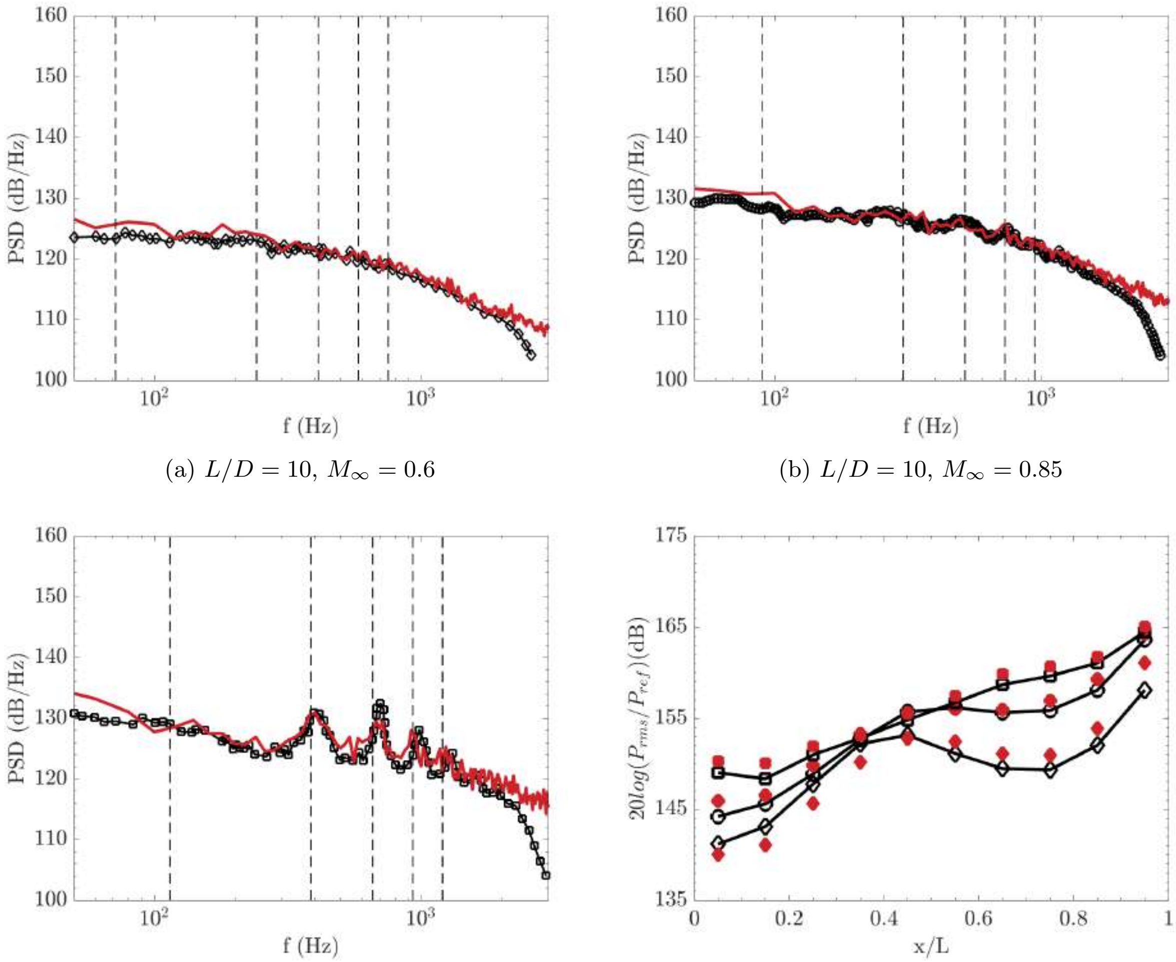

(a) $L/D = 10$, $M_\infty = 0.6$

(b) $L/D = 10$, $M_\infty = 0.85$

(c) $L/D = 10$, $M_\infty = 1.35$

(d) $L/D = 10$, P_{rms} distribution.

Figure 6: Kulite-averaged wall-pressure PSD and P_{rms} distribution along the cavity floor for the shallow $L/D = 10$ cavity configuration at Mach $M_\infty = 0.6$ ($-\diamond-$), 0.85 ($-\circ-$) and 1.35 ($-\square-$): **Experiment**; LES. The vertical lines represent the frequency of the first 5 Rossiter modes from equation 2.

measurements for both broadband and tonal noise over the full frequency range. The resonant frequencies are well captured by the semi-empirical equation 2, with $n = 2$ and 3 the dominant Rossiter modes for this configuration. The P_{rms} distribution on the cavity floor displays intense acoustic loads, gradually increasing in the streamwise direction, with maximum around 167 dB near the cavity aft wall (see figure 5(d)).

In contrast, when the cavity length-to-depth ratio is increased to $L/D = 10$ at the same $M_\infty = 0.85$ condition, the shear layer separating at the front wall no longer directly impinges the aft wall and instead tends to reattach on the cavity floor. This configuration is representative of closed-flow cavity, where there is no feedback loop and no resonant frequencies, as shown by the lack of clear Rossiter mode tones in the PSD in figure 6(b). The absence of intense flow-acoustic resonance mechanism also leads to a reduction in the wall-pressure broadband levels, especially in the lower frequency range $f \leq 1000$ Hz. The P_{rms} levels on the cavity floor are 4 to 10 dB lower than the levels in the deep (resonant) cavity $L/D = 5$ and the distribution now features a local maximum before the cavity half-length associated with the flow impingement on the cavity floor (see figure 6(d)).

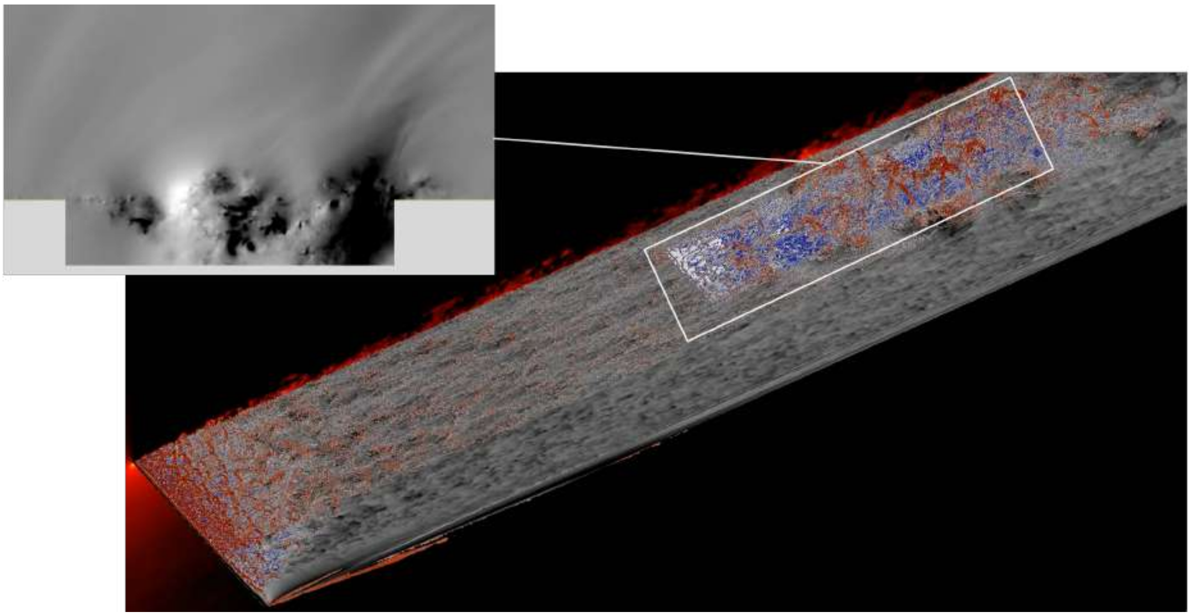

(a) Deep (resonant) cavity $L/D = 5$, $M_\infty = 0.85$

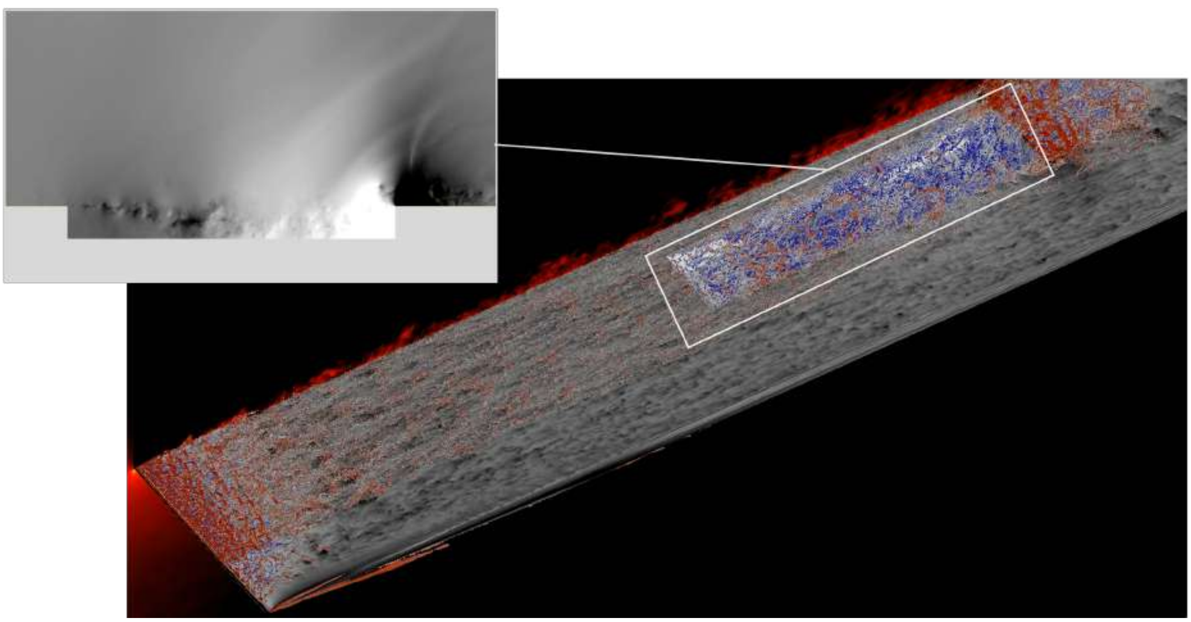

(b) Shallow (closed-flow) cavity $L/D = 10$, $M_\infty = 0.85$

Figure 7: Visualization of the pressure field ($0.9 \leq P/P_\infty \leq 1.1$, insert in grey scale) and flow field (Q-criterion colored by Mach number & surface shear stress) for the M219 deep and shallow cavity configuration at Mach $M_\infty = 0.85$, from the GPU-accelerated LES simulations on the refined grids.

B. Effects of Mach number

For the deep $L/D = 5$ cavity configuration, the flow-acoustic resonance mechanism is present at all conditions. The effect of increasing Mach number is to increase both broadband and tonal levels, to sharpen the cavity resonant tones and shift them to higher frequency. Overall, the resonant frequencies are well captured in the simulations, and closely match the frequencies of the Rossiter modes from the semi-empirical equation 2. Here, the best agreements with the semi-empirical predictions are at the subsonic conditions, with slightly more discrepancies observed at higher Mach number $M_\infty = 1.35$. Casalino *et al.* [17] proposed modifications to the equation 2 that take into account the reversed flow convective effects in the calculation of the backward acoustic propagation time, which they found to yield globally more accurate predictions of the resonance frequencies.

For the P_{rms} distribution on the cavity floor in figure 5(d)), the fluctuations steadily increase as a function of the streamwise location along the cavity at the subsonic conditions: the increase of M_∞ from 0.6 to 0.85 leads to higher P_{rms} levels by about 5-7 dB, consistent with the broadband and tone increase in the PSD. At the higher freestream Mach number 1.35, the P_{rms} distribution now exhibit more modulations and a local maximum in the middle of the cavity length. These features are associated with the standing-wave structure of the second Rossiter mode, which is dominant at this condition: as shown figure 5(c), the second Rossiter mode has a peak tone amplitude about 10dB larger than the next mode, and more than 20dB higher than the broadband levels. The modes spatial structure and visualization of the band-filtered pressure fluctuation are further discussed below in section IIIC.

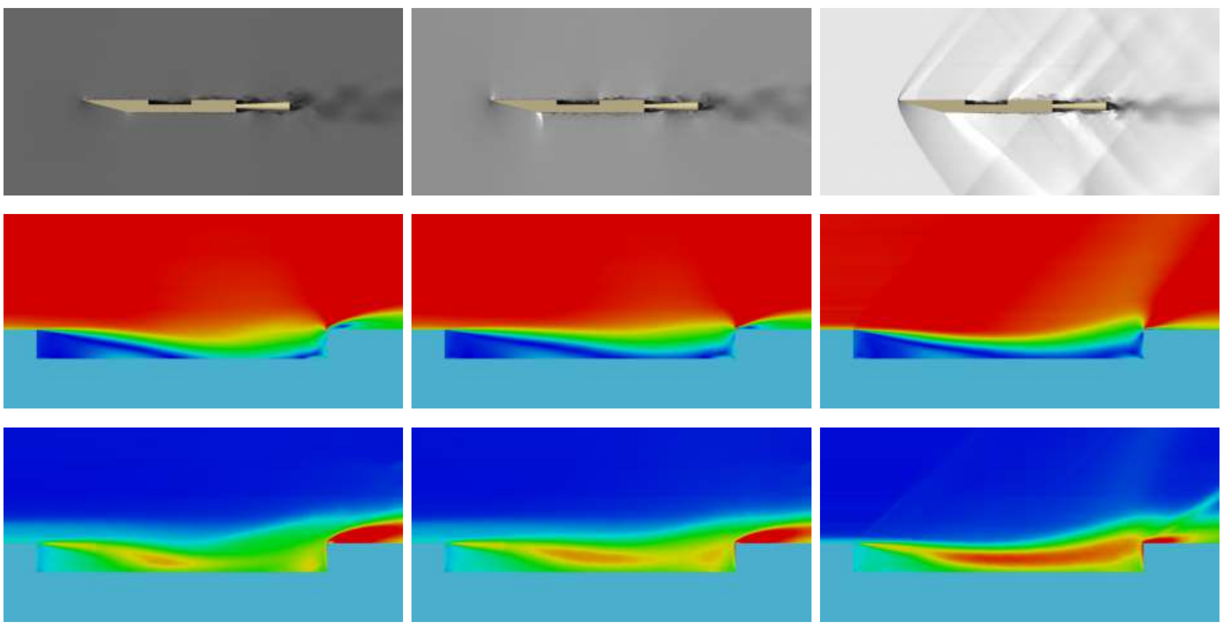

(a) $L/D = 10$, $M_\infty = 0.6$ (b) $L/D = 10$, $M_\infty = 0.85$ (c) $L/D = 10$, $M_\infty = 1.35$

Figure 8: Flow visualization in the midsection plane for the shallow $L/D = 10$ cavity configuration: instantaneous Mach number $0 \leq M \leq 1.5$ (top row), magnitude of time-averaged velocity $5 \leq |u_{avg}| \leq U_\infty$ m/s (middle row)) and of rms velocity $0 \leq |u_{rms}| \leq 0.35U_\infty$ m/s (bottom row).

In the experimental campaign of Tracy & Plentovich [29] for subsonic and transonic flow over rectangular cavities of various dimensions, the length-to-depth ratio $L/D = 10$ tends to be around the threshold where the flow regime gradually transitions from open- to closed-flow cavity, also referred to as transitional open/closed-flow cavity. To illustrate this transition when the Mach number is increased, figure 8 shows instantaneous flow visualization and velocity statistics in the midsection plane for the shallow $L/D = 10$ cavity configuration at the three operating conditions. At the lower Mach $M_\infty = 0.6$, the cavity is in the closed-flow regime, as described in the previous section: the flow separates from the upstream wall of the cavity, reattaches on the cavity floor and separates again near the downstream wall. There is no resonance and higher fluctuations are observed near where the flow impinges on the cavity floor. As the Mach number is increased to 0.85, the flow reattachment on the cavity floor is moved downstream and reduced. There is still no resonance but the spectra starts to exhibit small modulations at the expected Rossiter mode frequencies (see figure 6(b)). Finally, at supersonic condition $M_\infty = 1.35$, the main flow feature – aside from the shock and expansion waves around the model – is that there is now a small subsonic recirculation region inside the cavity, as the shear layer bends down without reattaching on the cavity floor and impinges on the downstream wall instead. The acoustic waves generated by the impingement can propagate upstream in the subsonic region of the flow and create new disturbances in the shear layer, leading to a weak resonance as shown in figure 6(c). The tone amplitudes and P_{rms} levels in the cavity are much lower than for the deep $L/D = 5$ configuration at the same Mach number. This cavity case is likely at the limit of the transitional to open-flow regime and is more subtle to capture in the simulations.

C. Effects of the cavity doors & dynamic deployment

To investigate the impact of the cavity doors, two additional simulations are performed for the deep $L/D = 5$ configurations at $M_\infty = 0.85$. First, the cavity with the opened doors is simulated using again the GPU-accelerated compressible flow solver on static grids. Then the dynamic deployment of the doors, from the fully closed to fully opened position described in section IIB, is simulated with the novel general-motion version of the solver.

First, figure 9 compares the wall-pressure PSD and the streamwise P_{rms} distribution for the configuration with and without doors on the static grids. Overall, the doors-open case is louder than the no-door case at every Kulite location, with differences of up to 10 dB. Unlike the no-door configuration where the second mode is dominant by only a few decibel, the presence of the doors amplifies the second mode tone amplitude ($\approx +10$dB) and attenuates the third mode (≈ -8dB), making the second mode substantially dominant. These trends are consistent with previous studies [9, 10, 11], which showed that the presence of doors generally elevates the overall noise level and modifies the relative contributions of the modes.

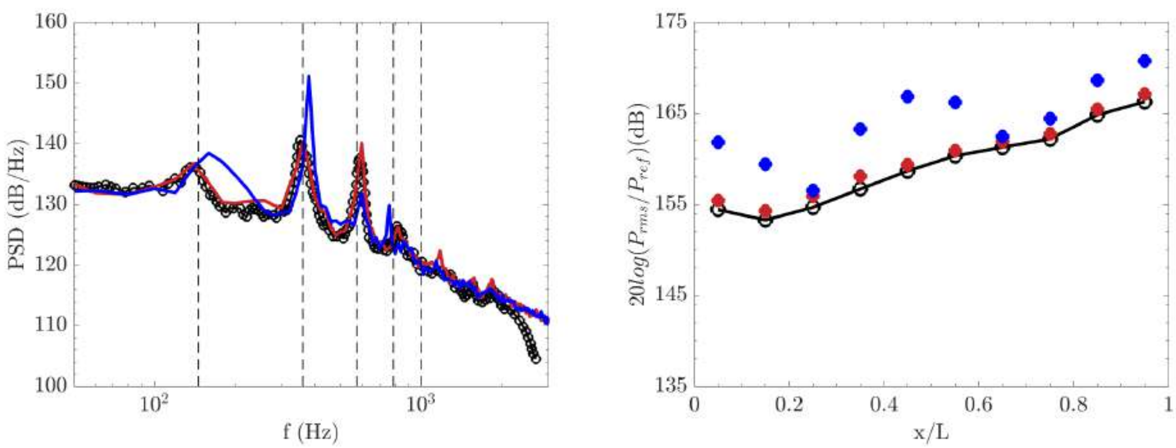

(a) $L/D = 5$, with & without doors

(b) P_{rms} distribution, with & without doors

Figure 9: Kulite-averaged wall-pressure PSD and P_{rms} distribution along the cavity floor for the deep $L/D = 5$ cavity configuration at Mach $M_\infty = 0.85$: **Experiment**; LES (no doors); LES (opened doors). The vertical lines represent the frequency of the first 5 Rossiter modes from equation 2.

.

To investigate the structure of the Rossiter modes, the band-filtered pressure fields on the cavity and surrounding surfaces at $M_\infty = 0.85$ are shown in figure 10 for both the static no-doors and doors-on configurations. The band-filtered diagnostic (also referred to as dBmap) is implemented as a GPU-resident streaming routine within the flow solver, incurring negligible computational cost and eliminating the need to store and post-process a large database of unsteady flow fields. The band-filtered analysis was performed at the first five Rossiter mode frequencies, $f = 146$, 360, 574, 788, and 1002 Hz, with a bandwidth of 50 Hz. These frequencies and bandwidth were chosen to capture the modes in both configurations, accommodating the slight frequency shift introduced by the doors.

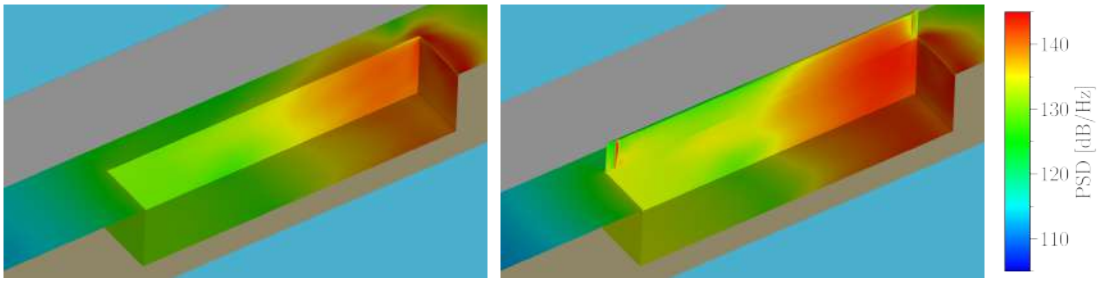

(a) Mode 1: $f = 146$ Hz

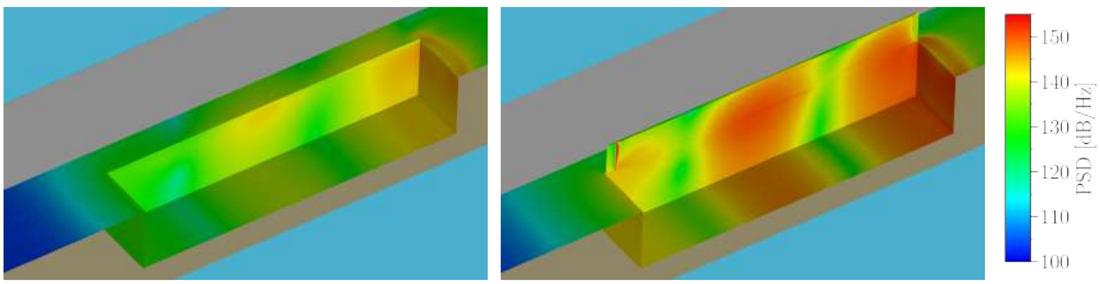

(b) Mode 2: $f = 360$ Hz

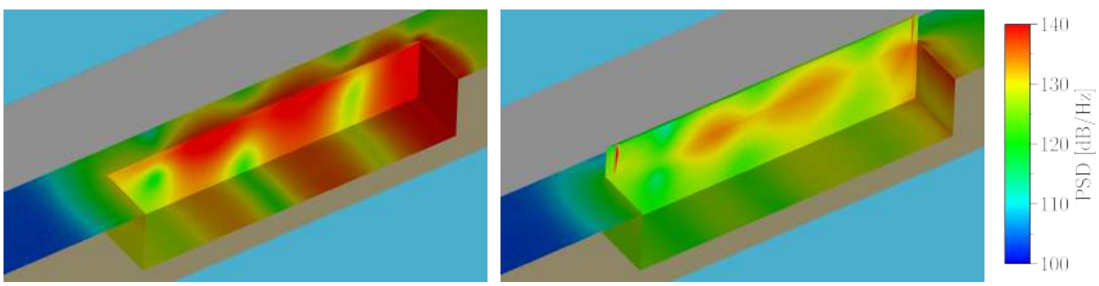

(c) Mode 3: $f = 574$ Hz

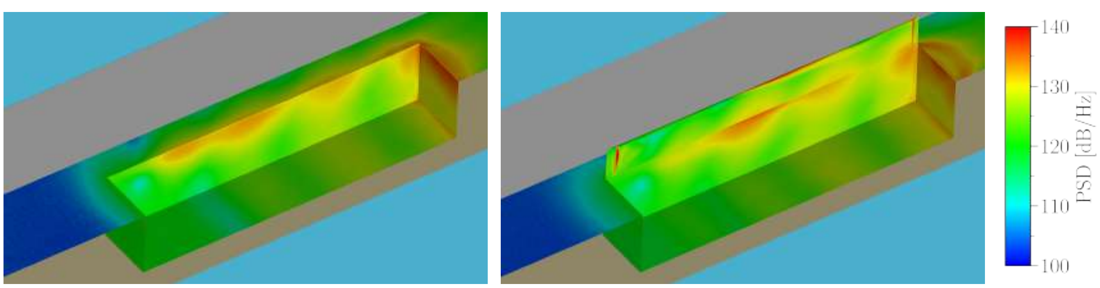

(d) Mode 4: $f = 788$ Hz

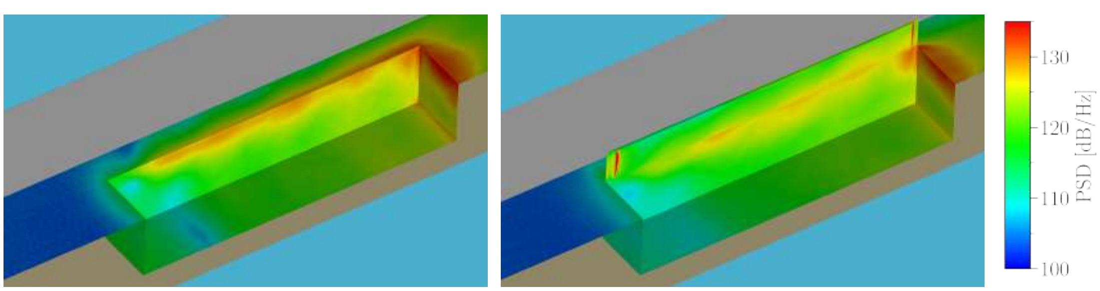

(e) Mode 5: $f = 1002$ Hz

Figure 10: Band-filtered PSD of surface pressure at the frequency of the Rossiter modes 1 to 5 for the deep $L/D = 5$ cavity configuration at $M_\infty = 0.85$. Left: no doors. Right: opened doors.

The band-filtered surface pressure fields in figure 10 reveal the standing-wave structure associated with each Rossiter mode. For modes n = 1–3, the number of nodes and anti-nodes within the cavity coincides with the mode index, consistent with previously reported results [30, 31]. For both configuration, there is an approximately constant strength along the side wall and floor of the cavity. In contrast, modes $n = 4$ and $n = 5$ are predominantly confined to the shear layer and do not imprint a coherent standing-wave pattern on the cavity floor. This localisation is consistent with the pressure spectra in figure 9a, in which modes 4 and 5 produce only a weak signature on the floor-mounted Kulite array.

The presence of the opened cavity doors introduces several notable changes. The spatial structure of mode 1 is largely preserved, with a slight increase in extent and amplitude, reminiscent of the enhanced, broader first Rossiter mode tone in figure 9a. Likewise, the spatial structure of mode 2 is mostly unchanged but the dB maps for the opened-door case highlight the substantial increase in amplitude observed in the wall-pressure PSD. By contrast, for Mode 3, both spatial structure and amplitude are strongly affected by the doors: the dB map levels decreases by approximately 10 dB, consistent with the tone reduction seen in figure 9a, and the mode becomes confined to the shear layer rather than extending down to the cavity floor as in the no-door configuration. As a results, the P_{rms} distribution along the cavity floor in figure 9b now reflects the spatial structure of the dominant Rossiter mode 2 when the opened doors are considered.

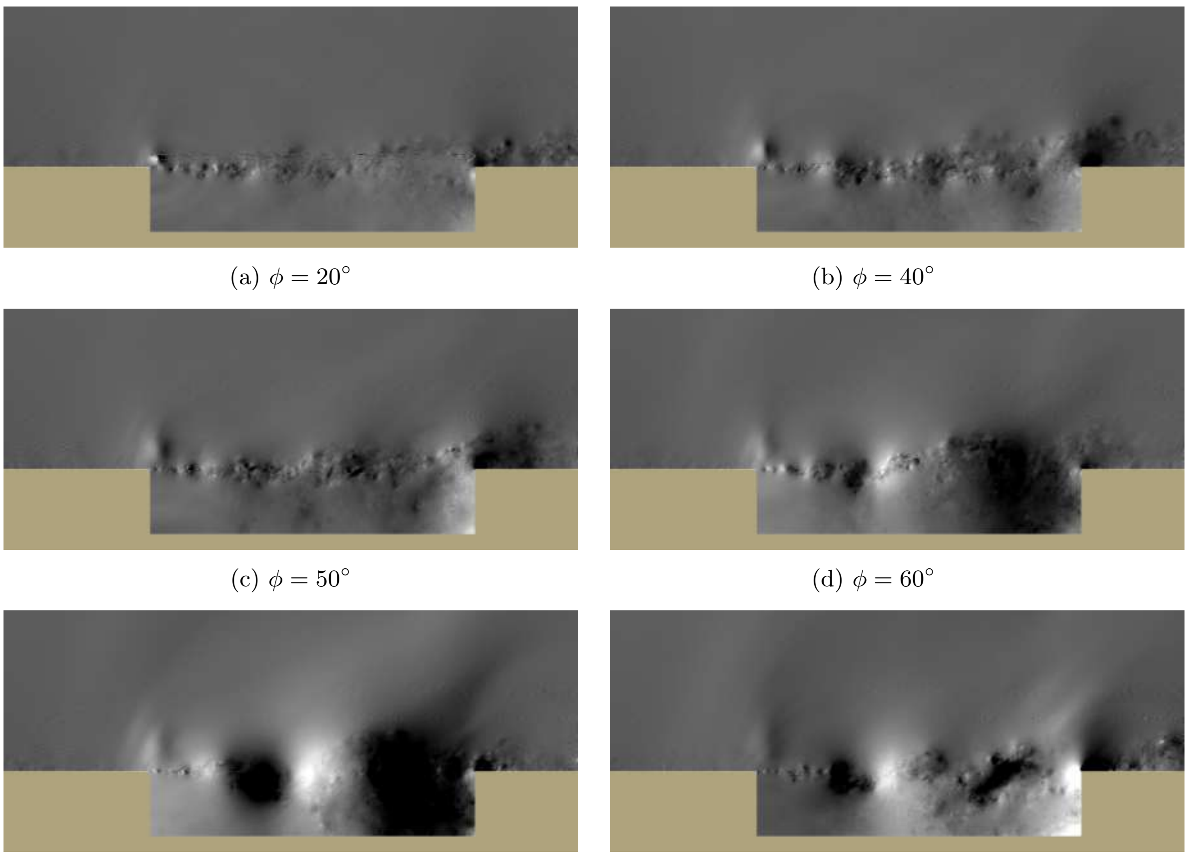

(a) $\phi = 20°$ (b) $\phi = 40°$

(c) $\phi = 50°$ (d) $\phi = 60°$

(e) $\phi = 70°$ (f) $\phi = 90°$

Figure 11: Visualization of the pressure field ($0.9 \leq P/P_\infty \leq 1.1$) along the center plane at various door angles ϕ for the moving-door cavity simulation ($L/D = 5$, $M_\infty = 0.85$).

Finally, the LES results for the opened-door static simulation are compared to data collected during the dynamic opening of the doors, rotating at a constant speed from the fully closed position ($\phi = 0°$) to the fully opened ($\phi = 90°$) position. Figure 11 displays the evolution of the cavity pressure field during door deployment, with the corresponding spectrogram from the Kulite on the cavity floor presented in figure 12. At shallow door angles (e.g., $\phi = 20°$), the flow fails to establish large-scale resonant structures, while at 60°, 70°, and 90°, the characteristic resonant waves are clearly visible. The transition between 30° and 60° marks a shift from a non-resonant regime dominated by small-scale structures to a developed resonant state featuring

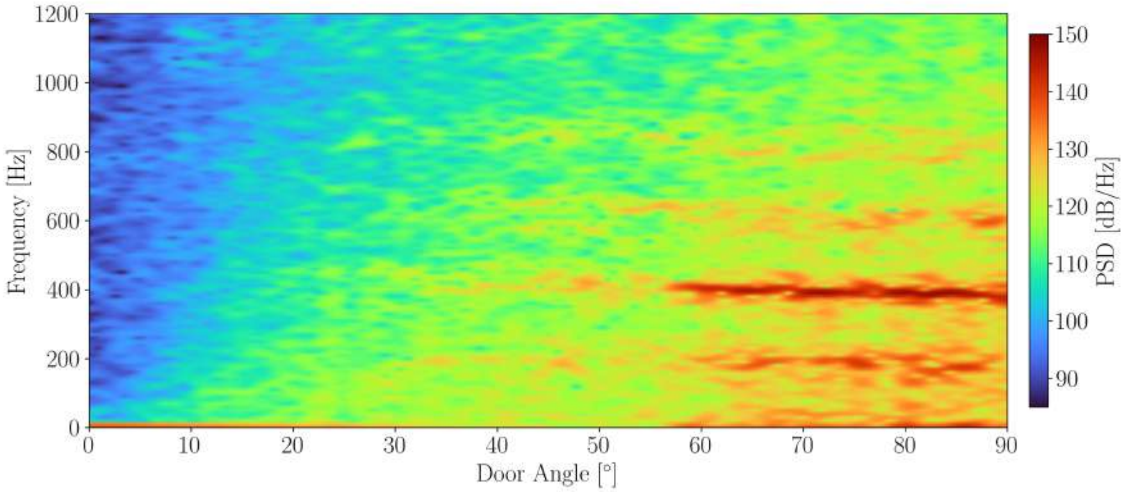

Figure 12: Time–frequency spectrogram of cavity wall-pressure fluctuations during door opening.

large-scale coherent structures spanning the cavity. This behaviour is mirrored in the spectrogram, where no strong tones are present for $\phi = 0°$ to $30°$, whereas pronounced tonal components emerge for $\phi \gtrsim 55°$, at frequencies matching the predictions from the Rossiter semi-empirical equation. Between $\phi \approx 30°$ and $55°$ a faint signature of the first two modes is detectable, but the resonant mechanism does not fully establish until the doors are sufficiently open. At these latter stages of the door deployment, the main features of the spectogram in figure 12 remain mostly unchanged with door angle and are consistent with the wall-pressure PSD results in figure 9a for the cavity with opened doors on static grids: the first 4 Rossiter modes are present with a clearly dominant resonance at mode 2 and a broader tone for mode 1.

IV. Conclusions

GPU-accelerated wall-modeled large-eddy simulations of the M219 cavity benchmark are performed at freestream Mach number $M_\infty = 0.6$, 0.85 and 1.35 for rectangular cavities of length-to-depth ratio $L/D = 5$ and $L/D = 10$. The full rig, sting support and wind-tunnel test section are included in the computational domain, with adiabatic wall-stress modeling on the solid surfaces and unstructured grids generated through the computation of Voronoi diagrams. Based on a preliminary grid resolution study, the refined meshes containing $\mathcal{O}(50)$ million control volumes are down-selected and used for all the conditions. This modest mesh size, combined with the performance of the GPU-accelerated flow solver on recent hardware, leads to small computational cost and high throughput: the collection of 0.5 s of statistics on the refined mesh required only ~ 15 GPU h on NVIDIA B200 GPUs.

Overall, wall-pressure predictions show good agreement with the measurements at Kulite transducers on the cavity floor, across all configurations and operating conditions. When self-sustained oscillations are present, the resonant frequencies are well captured and match the predictions from the Rossiter semi-empirical equation. The Kulite-averaged power spectral density matches the experimental data in terms of tone frequency, tone amplitude and broadband levels over $50 \leq f \leq 3000$ Hz, and the streamwise distribution of P_{rms} along the cavity floor is within ± 1 dB of the measurements at most Kulite location. The simulations also correctly capture the canonical change in flow regime with aspect ratio and freestream Mach number—a strong aeroacoustic resonance with clear Rossiter tones (modes $n = 2$ & 3 dominant) and high P_{rms} levels for the deep $L/D = 5$ configuration at all Mach numbers (characteristic of open-flow cavities), versus shear-layer reattachment on the cavity floor, no self-sustained resonance and significant reduction in floor P_{rms} for the shallow $L/D = 10$ configuration at subsonic Mach numbers (representative of closed-flow cavities)—as well as the onset of weak Rossiter resonance at the supersonic $M_\infty = 1.35$ condition for the $L/D = 10$ cavity (i.e., transitional open-flow cavities).

An additional simulation is conducted for the $L/D = 5$ cavity at $M_\infty = 0.85$ with generic doors in fully-opened position. The LES results suggest that the presence of the doors increases the floor P_{rms} levels,

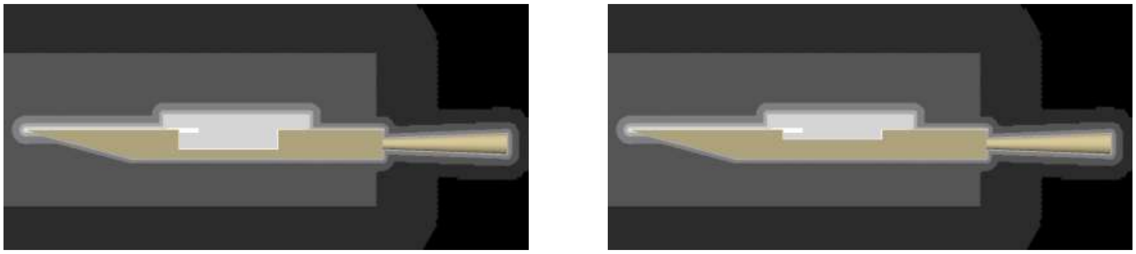

(a) Deep cavity $L/D = 5$

(b) Shallow cavity $L/D = 10$

Figure 13: Overview of the grid refinement strategy. The gray scale contours represent mesh resolution levels from 0.5 mm (light) to 32 mm (dark) for the refined grid.

slightly shifts the resonant tone frequencies and alters the dominant mode selection, consistent with trends reported in the literature. A GPU-resident band-filtered surface-pressure diagnostic at the first five Rossiter-mode frequencies shows that, with the opened doors, mode 2 preserved its standing-wave structure on the cavity floor while its amplitude increased substantially, whereas mode 3 was strongly attenuated and became confined to the shear layer rather than reaching the cavity floor. As a proof-of-concept demonstration of a novel general-motion version of the compressible flow solver, the dynamic deployment of the doors was also simulated, from fully-closed ($\phi = 0°$) to fully-opened ($\phi = 90°$) door positions. The time–frequency spectrogram of cavity wall-pressure fluctuation during the motion shows no resonance for door angles up to 30°, above which the first two Rossiter tones become detectable, with the resonant mechanism fully established when the doors are opened beyond 55°. For the remaining of the doors deployment, self-sustained oscillations are present in the cavity at the first 4 Rossiter mode, with a clear dominant mode 2, which is consistent with the results for the fully-opened door simulation.

Appendix - Grid resolution study

An preliminary grid resolution study was conducted at $M_\infty = 0.85$ for both the deep and shallow cavity configurations, and the meshing strategy is shown in figure 13. For the bulk of the volume inside the cavity, the grid spacing is set to 1 mm, which corresponds to approximately 50 to 100 cells per characteristic length D, consistent with the resolution typically used for other shear flows like jets [32, 33]. For the baseline mesh, near-wall refinement at 1 mm is also applied on the main surfaces, including all the cavity walls and the flap plate from the leading edge of the rig to 12 mm downstream of the aft cavity edge, for a width of approximately $2W$. This resolution yields $\mathcal{O}(10)$ cells across the incoming boundary layer thickness at the start of the cavity, assuming the development of a turbulent compressible boundary layer from the leading edge of the rig. Successive grid coarsening regions are then automatically generated as offsets of the surface and refinement windows, to progressively relax the mesh resolution away from the main zones of interest. For the refined mesh, the near-wall refinement is increased to 0.5 mm and a refinement zone is also added at that resolution for the first 20% for the cavity length to enclose initial shear-layer development. As part on the flow initialization, a coarse mesh was also used, with volume resolution set to 2 mm in the cavity. The mesh and simulation characteristics are summarized in Table 2 for the shallow cavity configuration: the resulting grid size for the coarse, baseline and refined mesh is approximately 14 million control volumes (Mcv), 25Mcv, and 51Mcv, respectively.

Mesh	**Size**	**Resolution**			**Time step**	**Computation cost**
		Cavity	**Walls**	**Shear-layer**		
Coarse	14 Mcv	2mm	1mm	2mm	1×10^{-6}s	2 GPUh
Baseline	25 Mcv	1mm	1mm	1mm	1×10^{-6}s	3.5 GPUh
Refined	51 Mcv	1mm	0.5mm	0.5mm	0.5×10^{-6}s	15 GPUh

Table 2: Summary of the grid resolution study parameters for the shallow $L/D = 10$ cavity configuration. The computational cost is reported for the collection of 0.5s of data on NVIDIA B200 GPUs.

The LES results from the coarse, baseline and refined mesh are compared to the Kulite measurements in figure 14 and 15, for the deep $L/D = 5$ and shallow $L/D = 10$ cavity, respectively. For $L/D = 5$, all three grids yields comparable results, in good agreement with the experiments in terms of prediction of tone frequency and amplitude, as well as broadband levels and streamwise distribution along the cavity floor. Even the coarse mesh used for flow initialization provided reasonable results. In contrast, for $L/D = 10$, the coarse mesh over-predicts the wall pressure fluctuations, in particular around $0.2 < x/L < 0.6$ where the flow tends to reattach on the cavity floor. In this case, there is only $\mathcal{O}(25)$ cells across the characteristic length D and the coarser 2mm resolution in the cavity is not sufficient to properly capture the initial shear-layer development. The predictions are improved for both the baseline and refined mesh, leading to good overall match with the measurements. Therefore, the refined mesh was down-selected to complete the analysis of the M219 cavity benchmark at all conditions.

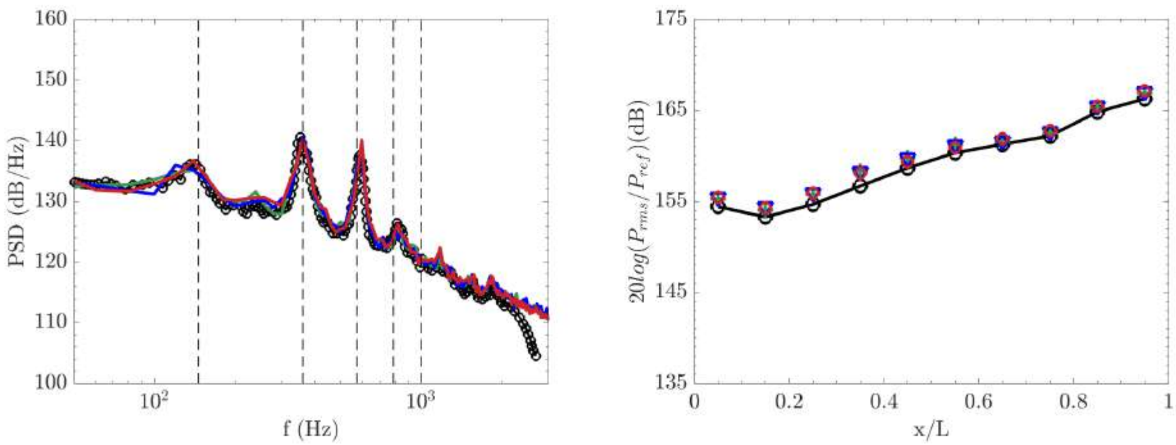

(a) Kulite-averaged wall-pressure PSD

(b) P_{rms} distribution

Figure 14: Comparisons with Kulite measurements for the deep $L/D = 5$ cavity configuration at Mach $M_\infty = 0.85$: **Experiment** (−○−), LES on the coarse, (——— ,+), baseline (——— ,∇) and refined (——— ,○) mesh. The vertical lines represent the frequency of the first 5 Rossiter modes from equation 2.

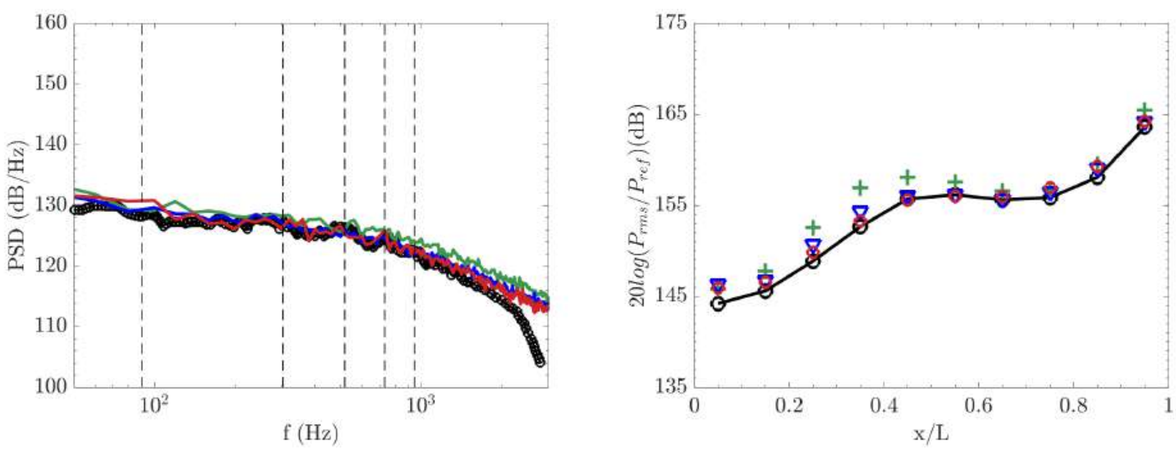

(a) Kulite-averaged wall-pressure PSD

(b) P_{rms} distribution

Figure 15: Comparisons with Kulite measurements for the shallow $L/D = 10$ cavity configuration at Mach $M_\infty = 0.85$: **Experiment** (−○−), LES on the coarse, (——— ,+), baseline (——— ,∇) and refined (——— ,○) mesh. The vertical lines represent the frequency of the first 5 Rossiter modes from equation 2.

Acknowledgments

Cadence - Cascade R&D acknowledges the DoD HPCMP and the NAVAIR Internal Flow modeling Team for their support on the testing of the GPU-accelerated compressible flow solver and its general-motion version.

References

[1] Lawson, S. J. and Barakos, G. N., "Review of numerical simulations for high-speed, turbulent cavity flows," *Progress in Aerospace Sciences*, Vol. 47, No. 3, 2011, pp. 186–216.

[2] Krishnamurty, K., "Acoustic radiation from two-dimensional rectangular cutouts in aerodynamic surfaces," Tech. Rep. NACA 3487, California Institute of Technology, 1955.

[3] Rossiter, J. E., "Wind–tunnel experiments on the flow over rectangular cavities at subsonic and transonic speeds," Tech. Rep. 3438, Aeronautical Research Council, London, UK, 1964.

[4] Heller, H. H., Holmes, D. G., and Covert, E. E., "Flow induced pressure oscillations in shallow cavities," *J. Sound Vib.*, Vol. 18(4), 1971, pp. 545–553.

[5] Rowley, C. W., Colonius, T., and Basu, A., "On self-sustained oscillations in two-dimensional compressible flow over rectangular cavities," *J. Fluid Mech.*, Vol. 455, 2002, pp. 315–346.

[6] Brès, G. A. and Colonius, T., "Three-dimensional instabilities in compressible flow over open cavities," *J. Fluid Mech.*, Vol. 599, 2008, pp. 309–339.

[7] Gonzalez-Martino, I., Viner, N., and Ben-Gida, H., "Very-large eddy simulations of transonic flows within a jet-fighter weapon bay with internal store," AIAA paper 2023-0057, 2023.

[8] Abuhanieh, S. and Akay, H. U., "Numerical investigation of store separation from cavity problems at high speeds," *Proceedings of the Institution of Mechanical Engineers, Part G: Journal of Aerospace Engineering*, Vol. 237, No. 16, 2023, pp. 3666–3680.

[9] Murray, N. E. and Jansen, B. J., "Effect of door configuration on cavity flow modulation process," *AIAA journal*, Vol. 50, No. 12, 2012, pp. 2932–2937.

[10] Sheta, E. F., Harris, R. E., George, B., Ukeiley, L., and Luke, E., "Loads and acoustics prediction on deployed weapons bay doors," *Journal of Vibration and Acoustics*, Vol. 139, No. 3, 2017, pp. 031007.

[11] Outten, B. and Kumar, R., "Effects of Door Opening Position on Cavity Flow Acoustics at Supersonic Speeds," *AIAA Journal*, Vol. 63, No. 6, 2025, pp. 2272–2285.

[12] Lawson, S. and Barakos, G., "Computational fluid dynamics analyses of flow over weapons-bay geometries," *Journal of Aircraft*, Vol. 47, No. 5, 2010, pp. 1605–1623.

[13] Loupy, G., Barakos, G., and Taylor, N., "Cavity flow over a transonic weapons bay during door operation," *Journal of Aircraft*, Vol. 55, No. 1, 2018, pp. 339–354.

[14] Henshaw, M. J. d. C., "Verification and validation data for computational unsteady aerodynamics," Tech. Rep. RTO-TR-26, AC/323(AVT)TP/19, NATO, 2000.

[15] Mancini, S., Kolb, A., Gonzalez-Martino, I., and Casalino, D., "Very-large eddy simulation of the M219 cavity at high-subsonic and supersonic conditions," AIAA paper 2019-1833, 2019.

[16] Mancini, S., Kolb, A., Gonzalez-Martino, I., and Casalino, D., "Predicting high-speed feedback mechanisms in rectangular cavities using lattice-Boltzmann very-large eddy simulations," *Aerospace Science and Technology*, Vol. 117, No. 106908, 2021.

[17] Casalino, D., Gonzalez-Martino, I., and Mancini, S., "On the Rossiter-Heller frequency of resonant cavities," *Aerospace Science and Technology*, Vol. 131, No. 108013, 2022.

[18] Chen, B. and Wang, Y., "Nonlinear numerical simulation for oscillating pressure in cavity and passive control research," *Int. J. of Aerospace Engineering*, Vol. 2019, No. 4153287, 2019.

[19] Larsson, J., Kawai, S., Bodart, J., and Bermejo-Moreno, I., "Large eddy simulation with modeled wall-stress: recent progress and future directions," *JSME Mech. Eng. Reviews*, Vol. 3, 2016.

[20] Bose, S. T. and Park, G. I., "Wall-modeled large-eddy simulation for complex turbulent flows," *Annual Review of Fluid Mechanics*, Vol. 50, 2018, pp. 535–561.

[21] Vreman, A., "An eddy-viscosity subgrid-scale model for turbulent shear flow: Algebraic theory and applications," *Physics of Fluids*, Vol. 16, Jan 2004, pp. 3670–3681.

[22] Brès, G. A., Bose, S. T., Emory, M., Ham, F. E., Schmidt, O. T., Rigas, G., and Colonius, T., "Large eddy simulations of co-annular turbulent jet using a Voronoi-based mesh generation framework," AIAA paper 2018-3302, 2018.

[23] Jain, N., Bravo, L., Kim, D., Murugan, M., Ghoshal, A., Ham, F., and Flatau, A., "Massively Parallel Large Eddy Simulation of Rotating Turbomachinery for Variable Speed Gas Turbine Engine Operation," *Energies*, Vol. 13, No. 3, 2020.

[24] Springel, V., "E pur si muove: Galilean-invariant cosmological hydrodynamical simulations on a moving mesh," *Monthly Notices of the Royal Astronomical Society*, Vol. 401, No. 2, 01 2010, pp. 791–851.

[25] Brès, G. A., Wang, K., Ivey, C. B., Bose, S. T., Okubo, G., Kamatsuchi, T., and Tanaka, H., "Predictions of fan noise and performance at transonic operating conditions using GPU-accelerated large-eddy simulations," AIAA paper 2024-3162, 2024.

[26] Wang, K., Bose, S. T., and Ivey, C., "GPU-accelerated full-wheel large-eddy simulations of a transonic fan stage," Proceedings of the ASME Turbo Expo, GT2024-128238, 2024.

[27] Brès, G. A., Wang, K., Ivey, C. B., Bose, S. T., Okubo, G., Kamatsuchi, T., and Tanaka, H., "GPU-accelerated large-eddy simulations for aeroacoustic predictions of a full-wheel multi-stage turbofan engine," AIAA paper 2025-3653, 2025.

[28] Afari, S., Brès, G. A., Wang, K., Thai, A., and Bain, J., "Performance and noise predictions of the Joby eVTOL propeller NFAC wind tunnel test using GPU-accelerated large-eddy simulations," Vertical Flight Society's 81st Forum, paper 81-2025-0085, 2025.

[29] Tracy, M. B. and Plentovich, E. B., "Cavity Unsteady-Pressure Measurements at Subsonic and Transonic Speeds," Tech. Rep. Technical Paper 3669, NASA, 1997.

[30] Zhang, Y., Cattafesta III, L. N., and Ukeiley, L., "Spectral analysis modal methods (SAMMs) using non-time-resolved PIV," *Experiments in Fluids*, Vol. 61, No. 11, 2020, pp. 226.

[31] Oka, Y., Ozawa, Y., Nagata, T., Asai, K., and Nonomura, T., "Experimental investigation of the supersonic cavity by spectral-POD of high-sampling rate pressure-sensitive paint data," *Experiments in Fluids*, Vol. 64, No. 5, 2023, pp. 108.

[32] Brès, G. A., Ham, F. E., Nichols, J. W., and Lele, S. K., "Unstructured Large Eddy Simulations of Supersonic Jets," *AIAA J.*, Vol. 55, No. 4, 2017, pp. 1164–1184.

[33] Brès, G. A., Jordan, P., Jaunet, V., Le Rallic, M., Cavalieri, A. V. G., Towne, A., Lele, S. K., Colonius, T., and Schmidt, O. T., "Importance of the nozzle-exit boundary-layer state in subsonic turbulent jets," *J. Fluid Mech.*, Vol. 851, 2018, pp. 83–124.